Gate voltage induced injection and shift currents in AA- and AB-stacked bilayer graphene

Ze Zheng, Kainan Chang,* and Jin Luo Cheng†

GPL Photonics Laboratory, State Key Laboratory of Luminescence and Applications, Changchun Institute of Optics, Fine Mechanics and Physics, Chinese Academy of Sciences, Changchun, Jilin 130033, People's Republic of China and University of Chinese Academy of Sciences, Beijing 100039, China

(Received 3 August 2023; revised 9 November 2023; accepted 14 November 2023; published 4 December 2023)

Generating photogalvanic effects in centrosymmetric materials can provide new opportunities for developing passive photodetectors and energy-harvesting devices. In this work, we investigate the photogalvanic effects in centrosymmetric two-dimensional materials, AA- and AB-stacked bilayer graphene, by applying an external gate voltage to break the inversion symmetry. Using a tight-binding model to describe the electronic states, the injection coefficients for circular photogalvanic effects and shift conductivities for linear photogalvanic effects are calculated for both materials with light wavelengths ranging from terahertz to visible. We find that gate voltage induced photogalvanic effects can be very significant for AB-stacked bilayer graphene, generating a maximal dc current on the order of milliamperes for a 1 μm wide sample illuminated by a light intensity of $0.1\,\mathrm{GW/cm^2}$, which is determined by the optical transition around the band gap and van Hove singularity points. Although such effects in AA-stacked bilayer graphene are about two orders of magnitude smaller than those in AB-stacked bilayer graphene, the spectrum is interestingly limited in a very narrow photon energy window, which is associated with the interlayer coupling strength. A detailed analysis of the light polarization dependence is also performed. The gate voltage and chemical potential can be used to effectively control the photogalvanic effects.

DOI: 10.1103/PhysRevB.108.235401

I. INTRODUCTION

Photogalvanic effects are nonlinear optical responses that generate direct currents in homogeneous materials, and such a passive process is considered a direct and powerful photoelectric conversion method [1–3]. The widely discussed photogalvanic effects can be induced by one-color injection current and shift current, which can be excited by light with one wavelength and are second order nonlinear optical processes occurring in noncentrosymmetric materials, or two-color coherent current injection, which is excited by light with two different wavelengths [4–6] and can be third (for "1+2" process) [7] or fifth (for "2+3" process) [8] order nonlinear optical processes insensitive to the inversion symmetry of materials. According to the response to the light polarization, second order photogalvanic effects are also phenomenologically divided into the circularly polarized photogalvanic effect and the linearly polarized photogalvanic effect; the latter is light phase insensitive and can be used for solar energy harvesting without forming $p-n$ junctions to surpass the Shockley-Queisser limit [9–11]. One of the research topics in this field is to find materials with significant photogalvanic effects in a specific frequency range, and several studies have been conducted on various new materials, including two-dimensional (2D) materials [12–16], Dirac or Weyl semimetals [1,17,18], ferroelectric materials [19–22], and so on.

As the first two-dimensional material, graphene is a potential candidate for realizing new functionality in optoelectronic devices because its superior optical and electronic properties exceed those of many traditional bulk materials. However, because of its centrosymmetric crystal structure, one-color injection and shift currents vanish in many types of few-layer graphene as well as their nanostructures, whereas two-color coherent control has been well studied in both theories [7,23–25] and experiments [26,27]. It is still meaningful to generate one-color injection and shift currents in centrosymmetric graphene based structures in order to utilize its extraordinary physical properties. The generation of second order response can be realized by forming an asymmetric interface or edge [28], applying an external electric field [29], forming surface curvature [30], considering the spatial variation of the light field [31], and stacking graphene layers into an asymmetric structure [32]. Wei *et al.* [12] studied the gate field induced injection and shift currents in zigzag graphene nanoribbons and found that the subband and edge states determine the generated currents with an effective modulation of their amplitudes by the ribbon width and the static field strength. Xiong *et al.* [33] investigated the light polarization dependence of in-plane shift current in an AB-stacked bilayer graphene (AB-BG) by applying a gate voltage, and their results clearly illustrated a sizable photocurrent at a given light frequency; however, neither the spectra of the shift conductivity nor the injection current was present. By stacking two layers of monolayer graphene with a relative rotation to form twisted bilayer graphene, a large shift current can be produced due to the huge density of states when the flat band is formed at magic

*knchang@ciomp.ac.cn
†jlcheng@ciomp.ac.cn

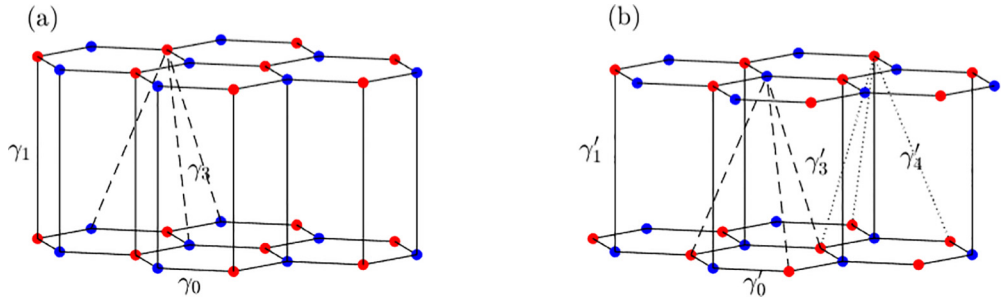

FIG. 1. Crystal structures and tight-binding hopping parameters for (a) AA-BG and (b) AB-BG.

angles [15,16,34]. Surprisingly, whether the gate voltage can generate a photogalvanic effect in AA-stacked bilayer graphene (AA-BG) is still not clear.

In this paper, we systematically study the spectra of the injection coefficients and shift conductivities of AA-BG and AB-BG after applying a gate voltage to break the inversion symmetry, as well as their dependence on the gate voltage and chemical potential. Their electronic states are described by a widely adopted tight-binding model formed by the carbon $2p_z$ orbitals [29,35], and the expressions for the injection coefficient and shift conductivity are taken from Ref. [36]. After confirming the results from Xiong *et al.* [33], for AB-BG we also provide detailed spectra for all tensor components of injection coefficients and shift conductivities and analyze the contributions from different optical transitions. A maximal current on the order of milliamperes can be generated in AB-BG for a 1 μm wide sample at a light intensity of $0.1\,\mathrm{GW/cm^2}$. These details will be helpful in the experimental design. For comparison, the photogalvanic effects in AA-BG are also presented with analytic expressions under the linear dispersion approximation, and the response can occur only in a very narrow photon energy range. Our results show the stacking order can induce huge differences in the photogalvanic coefficients and confirm the feasibility of generating photogalvanic effects in AA-BG and AB-BG.

This paper is organized as follows. In Sec. II we introduce the tight-binding models for AA-BG and AB-BG after applying a gate voltage and give the expressions for the injection coefficient and shift conductivity. In Sec. III we present the spectra of the injection coefficient and shift conductivity for AA-BG and AB-BG and discuss the effects of the gate voltage and chemical potential. We conclude in Sec. IV.

II. MODELS

A. Hamiltonian

We consider the tight-binding Hamiltonian for AA-BG and AB-BG, whose crystal structures are illustrated in Figs. 1(a) and 1(b), respectively. These two structures have the same primitive lattice vectors $\boldsymbol{a}_1 = a_0(\frac{1}{2}\hat{\boldsymbol{x}} + \frac{\sqrt{3}}{2}\hat{\boldsymbol{y}})$ and $\boldsymbol{a}_2 = a_0(-\frac{1}{2}\hat{\boldsymbol{x}} + \frac{\sqrt{3}}{2}\hat{\boldsymbol{y}})$, with the lattice constant $a_0 = 2.46$ Å. The atomic positions in the unit cell are taken as $\boldsymbol{\tau}_A = \boldsymbol{0}$, $\boldsymbol{\tau}_B = (\boldsymbol{a}_1 + \boldsymbol{a}_2)/3$, $\boldsymbol{\tau}_{A'} = c\hat{\boldsymbol{z}}$, and $\boldsymbol{\tau}_{B'} = \boldsymbol{\tau}_B + c\hat{\boldsymbol{z}}$ for AA-BG and $\boldsymbol{\tau}_A = \boldsymbol{0}$, $\boldsymbol{\tau}_B = (\boldsymbol{a}_1 + \boldsymbol{a}_2)/3$, $\boldsymbol{\tau}_{A'} = \boldsymbol{\tau}_B + c\hat{\boldsymbol{z}}$, and $\boldsymbol{\tau}_{B'} = 2\boldsymbol{\tau}_B + c\hat{\boldsymbol{z}}$ for AB-BG, where $c = 3.35$ Å is the interlayer distance. The primitive reciprocal lattice vectors are $\boldsymbol{b}_1 = \frac{2\pi}{a_0}(\hat{\boldsymbol{x}} + \frac{1}{\sqrt{3}}\hat{\boldsymbol{y}})$ and $\boldsymbol{b}_2 = \frac{2\pi}{a_0}(-\hat{\boldsymbol{x}} + \frac{1}{\sqrt{3}}\hat{\boldsymbol{y}})$. The electronic states are described by a tight-binding model employing carbon $2p_z$ orbitals. The unperturbed Hamiltonian [35] for AA-BG is

$$H_{\boldsymbol{k}}^{\mathrm{AA}} = \begin{pmatrix} -\Delta & \gamma_0 g_{\boldsymbol{k}} & \gamma_1 & \gamma_3 g_{\boldsymbol{k}} \\ \gamma_0 g_{\boldsymbol{k}}^* & -\Delta & \gamma_3 g_{\boldsymbol{k}}^* & \gamma_1 \\ \gamma_1 & \gamma_3 g_{\boldsymbol{k}} & \Delta & \gamma_0 g_{\boldsymbol{k}} \\ \gamma_3 g_{\boldsymbol{k}}^* & \gamma_1 & \gamma_0 g_{\boldsymbol{k}}^* & \Delta \end{pmatrix}. \tag{1}$$

Here $\boldsymbol{k}$ is the electron wave vector, and $g_{\boldsymbol{k}} = 1 + e^{-i\boldsymbol{k}\cdot\boldsymbol{a}_1} + e^{-i\boldsymbol{k}\cdot\boldsymbol{a}_2}$. The hopping parameters are illustrated in Fig. 1(a), with $\gamma_0 = 2.569\,\mathrm{eV}$, $\gamma_1 = 0.361\,\mathrm{eV}$, and $\gamma_3 = -0.032\,\mathrm{eV}$. The on-site energies $\pm\Delta$ can be experimentally induced either by a gate voltage by using the electrostatic gating method and choosing the electrode to be an electrolyte [37] or a 2D material [38] or by adjusting the carrier concentration of each layer from charge doping [39]. The Hamiltonian for AB-BG is taken from Ref. [29] as

$$H_{\boldsymbol{k}}^{\mathrm{AB}} = \begin{pmatrix} -\Delta - \frac{\Delta'}{2} & \gamma_0' g_{\boldsymbol{k}} & \gamma_4' g_{\boldsymbol{k}} & \gamma_3' g_{\boldsymbol{k}}^* \\ \gamma_0' g_{\boldsymbol{k}}^* & -\Delta + \frac{\Delta'}{2} & \gamma_1' & \gamma_4' g_{\boldsymbol{k}} \\ \gamma_4' g_{\boldsymbol{k}}^* & \gamma_1' & \Delta + \frac{\Delta'}{2} & \gamma_0' g_{\boldsymbol{k}} \\ \gamma_3' g_{\boldsymbol{k}} & \gamma_4' g_{\boldsymbol{k}}^* & \gamma_0' g_{\boldsymbol{k}}^* & \Delta - \frac{\Delta'}{2} \end{pmatrix}, \tag{2}$$

where the hopping parameters [see Fig. 1(b)] are $\gamma_0' = -3.16\,\mathrm{eV}$, $\gamma_1' = 0.381\,\mathrm{eV}$, $\gamma_3' = -0.38\,\mathrm{eV}$, and $\gamma_4' = 0.14\,\mathrm{eV}$. The on-site potential difference $\Delta' = 0.022\,\mathrm{eV}$ is induced by the asymmetric environment of the A and B atoms in the crystal structure.

The eigenstates $C_{n\boldsymbol{k}}$ and eigenenergies $\epsilon_{n\boldsymbol{k}}$ at the nth band are obtained by diagonalizing the Hamiltonian through

$$H_{\boldsymbol{k}} C_{n\boldsymbol{k}} = \epsilon_{n\boldsymbol{k}} C_{n\boldsymbol{k}}. \tag{3}$$

The calculation of the optical responses involves the position operator $\widetilde{\boldsymbol{r}}_{\boldsymbol{k}}$ and velocity operator $\widetilde{\boldsymbol{v}}_{\boldsymbol{k}}$, which are

$$\widetilde{\boldsymbol{r}}_{\boldsymbol{k}} = i\boldsymbol{\nabla}_{\boldsymbol{k}} + \begin{pmatrix} \boldsymbol{\tau}_A & 0 & 0 & 0 \\ 0 & \boldsymbol{\tau}_B & 0 & 0 \\ 0 & 0 & \boldsymbol{\tau}_{A'} & 0 \\ 0 & 0 & 0 & \boldsymbol{\tau}_{B'} \end{pmatrix}, \quad \widetilde{\boldsymbol{v}}_{\boldsymbol{k}} = \frac{1}{i\hbar}[\widetilde{\boldsymbol{r}}_{\boldsymbol{k}}, H_{\boldsymbol{k}}], \tag{4}$$

respectively. The matrix elements of the position operator give the Berry connections $\boldsymbol{\xi}_{nm\boldsymbol{k}}$ as

$$\boldsymbol{\xi}_{nm\boldsymbol{k}} = C_{n\boldsymbol{k}}^{\dagger} \widetilde{\boldsymbol{r}}_{\boldsymbol{k}} C_{m\boldsymbol{k}}, \tag{5}$$

and those of the velocity operator are calculated as $\boldsymbol{v}_{nmk} = C^{\dagger}_{nk}\widetilde{\boldsymbol{v}}_{\boldsymbol{k}}C_{mk}$. Due to the derivative with respect to the wave vector $\boldsymbol{k}$, a direct calculation of $\boldsymbol{\xi}_{nmk}$ from Eq. (5) requires that the wave function C_{nk} is a smooth function of $\boldsymbol{k}$. However, this becomes quite difficult in numerical calculation because the phase is arbitrary for a numerical wave function. Practically, the off-diagonal terms of $\boldsymbol{\xi}_{nmk}$ can be also calculated from the velocity operator as

$$\boldsymbol{r}_{nmk} = \begin{cases} \boldsymbol{\xi}_{nmk} = \frac{\boldsymbol{v}_{nmk}}{i\omega_{nmk}} & (n \neq m), \\ 0 & (n = m), \end{cases} \tag{6}$$

with $\hbar\omega_{nmk} = \epsilon_{nk} - \epsilon_{mk}$. The diagonal terms ξ^{a}_{nnk} usually appear in the generalized derivative of $(r^{c}_{\boldsymbol{k}})_{;nmk^{a}} = \frac{\partial r^{c}_{nmk}}{\partial k^{a}} - i(\xi^{a}_{nnk} - \xi^{a}_{mmk})r^{c}_{nmk}$, which is alternatively calculated [12] as

$$\left(r^{c}_{\boldsymbol{k}}\right)_{;nmk^{a}} = \frac{-ir^{c}_{nmk}\mathcal{V}^{a}_{mnk} + \hbar M^{ca}_{nmk} + i\left[r^{a}_{\boldsymbol{k}}, v^{c}_{\boldsymbol{k}}\right]_{nm}}{i\omega_{nmk}}, \tag{7}$$

with $\mathcal{V}^{a}_{mnk} = v^{a}_{mmk} - v^{a}_{nnk} = \frac{\partial\omega_{mnk}}{\partial k^{a}}$ and

$$M^{ca}_{nmk} = C^{\dagger}_{nk}\frac{1}{i\hbar}\left[\widetilde{r}^{a}_{\boldsymbol{k}}, \widetilde{v}^{c}_{\boldsymbol{k}}\right]C_{mk}, \tag{8}$$

where the Roman letters a and c indicate the Cartesian directions x, y, and z. Note that the electron wave vector has only in-plane components x and y, and the derivative $\frac{\partial}{\partial k^{z}}$ thus gives zero and $(r^{a}_{\boldsymbol{k}})_{;nmk^{z}} = -i(\xi^{z}_{nnk} - \xi^{z}_{mmk})r^{a}_{nmk}$.

B. Injection and shift currents

We focus on the injection and shift currents induced by a laser pulse centered at frequency ω, for which the electric field is $\boldsymbol{E}(t) = \boldsymbol{E}_0(t)e^{-i\omega t} + \text{c.c.}$ and $\boldsymbol{E}_0(t)$ is a slowly varying envelope function. The response static currents can be written as

$$\boldsymbol{J}_0(t) = \boldsymbol{J}_{\text{inj}}(t) + \boldsymbol{J}_{\text{sh}}(t). \tag{9}$$

Here the first term $\boldsymbol{J}_{\text{inj}}(t)$ is a one-color injection current satisfying

$$\frac{dJ^{a}_{\text{inj}}(t)}{dt} = 2i\eta^{abc}(\omega)E^{b}_0(t)\left[E^{c}_0(t)\right]^{*}, \tag{10}$$

with the injection coefficient $\eta^{abc}(\omega)$ given by

$$\eta^{abc}(\omega) = \frac{2e^{3}\pi}{\hbar^{2}}\int\frac{d\boldsymbol{k}}{4\pi^{2}}\sum_{nm}\mathcal{V}^{a}_{mnk}f_{nmk} \times \text{Im}\left[r^{c}_{mnk}r^{b}_{nmk}\right]\delta(\omega_{mnk} - \omega). \tag{11}$$

Here $f_{nmk} = f_{nk} - f_{mk}$ is the population difference, with the Fermi-Dirac distribution $f_{nk} = [1 - e^{(\epsilon_{nk}-\mu)/k_BT}]^{-1}$ for a given chemical potential μ and temperature T. The second term, $\boldsymbol{J}_{\text{sh}}(t)$, in Eq. (9) is a shift current, written as

$$J^{a}_{\text{sh}}(t) = 2\sigma^{abc}(\omega)E^{b}_0(t)\left[E^{c}_0(t)\right]^{*}, \tag{12}$$

with the shift conductivity $\sigma^{abc}(\omega)$ given by

$$\sigma^{abc}(\omega) = -\frac{i\pi e^{3}}{\hbar^{2}}\int\frac{d\boldsymbol{k}}{4\pi^{2}}\sum_{nm}f_{nmk}\left[r^{b}_{mnk}\left(r^{c}_{\boldsymbol{k}}\right)_{;nmk^{a}} + r^{c}_{mnk}\left(r^{b}_{\boldsymbol{k}}\right)_{;nmk^{a}}\right]\delta(\omega_{mnk} - \omega). \tag{13}$$

Further discussion of photocurrents starts with a symmetry analysis of the tensors of $\eta^{abc}(\omega)$ and $\sigma^{abc}(\omega)$. The presence of time-reversal symmetry gives $\boldsymbol{r}_{nmk} = \boldsymbol{r}_{mn(-\boldsymbol{k})} = [\boldsymbol{r}_{nm(-\boldsymbol{k})}]^{*}$, $\boldsymbol{v}_{nmk} = -\boldsymbol{v}_{mn(-\boldsymbol{k})} = -[\boldsymbol{v}_{nm(-\boldsymbol{k})}]^{*}$, $\epsilon_{nk} = \epsilon_{n(-\boldsymbol{k})}$, and $(r^{b}_{\boldsymbol{k}})_{;nmk^{a}} = -(r^{b}_{-\boldsymbol{k}})_{;mnk^{a}} = -[(r^{b}_{\boldsymbol{k}})_{;nmk^{a}}]^{*}$. Thus, from Eqs. (11) and (13), we obtain $\eta^{abc} = [\eta^{abc}]^{*}$ and $\sigma^{abc} = [\sigma^{abc}]^{*}$, which are both real numbers. At finite gate voltage, the crystal point group of AB-BG is C_{3v}, whose symmetry is lower than that of AA-BG with crystal point group C_{6v}. Thus, we can check the symmetry properties of AB-BG first and then refine them to AA-BG. Combining the point group and the time reversal symmetry, the nonzero tensor components satisfy $\eta^{xzx} = \eta^{yzy} = \eta^{xxz} = \eta^{yyz}$, $\sigma^{xzx} = \sigma^{yzy} = \sigma^{xxz} = \sigma^{yyz}$, $\sigma^{zxx} = \sigma^{zyy}$, σ^{zzz}, and $\sigma^{yyy} = -\sigma^{yxx} = -\sigma^{xxy} = -\sigma^{xyx}$. Then the injection current becomes

$$\frac{dJ^{a}_{\text{inj}}(t)}{dt} = 4\eta^{xzx}(\omega)\text{Im}\left\{E^{a}_0(t)\left[E^{z}_0(t)\right]^{*}\right\}(1 - \delta_{a,z}), \tag{14}$$

and the shift current is

$$J^{x}_{\text{sh}}(t) = 4\sigma^{xzx}(\omega)\text{Re}\left\{E^{z}_0(t)\left[E^{x}_0(t)\right]^{*}\right\} - 4\sigma^{yyy}(\omega)\text{Re}\left\{E^{x}_0(t)\left[E^{y}_0(t)\right]^{*}\right\}, \tag{15a}$$

$$J^{y}_{\text{sh}}(t) = 4\sigma^{xzx}(\omega)\text{Re}\left\{E^{z}_0(t)\left[E^{y}_0(t)\right]^{*}\right\} + 2\sigma^{yyy}(\omega)\left[\left|E^{y}_0(t)\right|^{2} - \left|E^{x}_0(t)\right|^{2}\right], \tag{15b}$$

$$J^{z}_{\text{sh}}(t) = 2\sigma^{zxx}(\omega)\left[\left|E^{x}_0(t)\right|^{2} + \left|E^{y}_0(t)\right|^{2}\right] + 2\sigma^{zzz}(\omega)\left|E^{z}_0(t)\right|^{2}. \tag{15c}$$

For AA-BG, the results are similar, except that the σ^{yyy} component disappears due to the extra crystal symmetry.

The injection current in AA-BG or AB-BG requires an elliptically polarized obliquely incident light, and its z component vanishes due to the lack of freely moving electrons along this quantum confined direction. The z component of the shift current in AA-BG or AB-BG, induced by the charge shift between the two layers under light excitation, can always be generated. Such a shift current can lead to charge accumulation between these two layers, which can further induce a gate voltage in this system, as discussed by Gao *et al.* [40]. The in-plane components of the shift current in AA-BG can be generated only for an elliptically polarized light that is obliquely incident, while those in AB-BG have no such limit. In doped systems, although Eq. (13) includes the Pauli blocking effect, the Fermi surface can have an additional contribution to the shift conductivity, as shown in the works by de Juan *et al.* [41] and Gao *et al.* [42]. Our numerical results indicate that this contribution is negligible compared to those in Eq. (13), and thus, it is ignored in this work.

III. RESULTS

A. Analytical results for AA-BG

The Hamiltonian for AA-BG can be analytically diagonalized. The eigenstates are

$$C_{nk} = \frac{\sqrt{1 - \alpha_n\mathcal{N}_{\beta_n k}}}{2\sqrt{2}}\begin{pmatrix} -\hat{g}_{\boldsymbol{k}} \\ -\beta_n \\ \beta_n\hat{g}_{\boldsymbol{k}} \\ 1 \end{pmatrix} + \frac{\alpha_n\sqrt{1 + \alpha_n\mathcal{N}_{\beta_n k}}}{2\sqrt{2}}\begin{pmatrix} \hat{g}_{\boldsymbol{k}} \\ \beta_n \\ \beta_n\hat{g}_{\boldsymbol{k}} \\ 1 \end{pmatrix}, \tag{16}$$

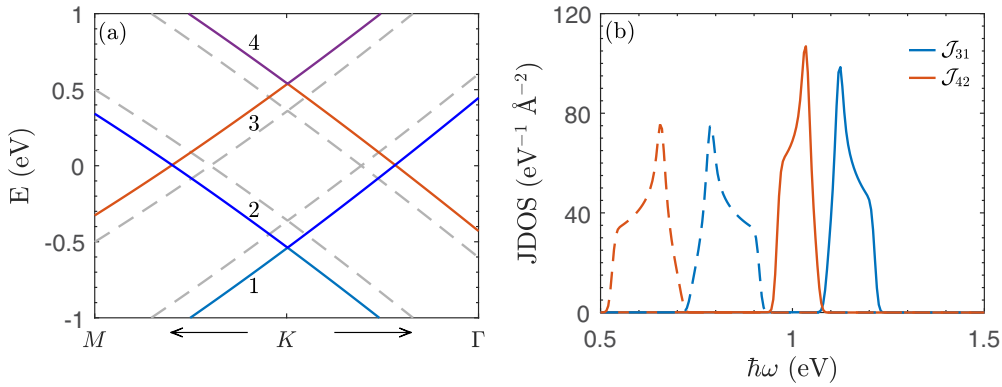

FIG. 2. (a) Band structure and (b) JDOS for AA-BG at $\Delta = 0$ (dashed curves) and $\Delta = 0.4$ eV (solid curves).

with $\hat{g}_k = g_k/|g_k|$ and

$$\mathcal{N}_{\beta_n k} = \frac{\gamma_3|g_k| + \beta_n\gamma_1}{\sqrt{\Delta^2 + (\gamma_3|g_k| + \beta_n\gamma_1)^2}}. \tag{17}$$

Here $n = 1, 2, 3, 4$ denotes the band index, with $\alpha_n = -1, -1, +1, +1$ and $\beta_n = -1, +1, -1, +1$, respectively. The associated eigenenergies are

$$\epsilon_{nk} = \beta_n\gamma_0|g_k| + \alpha_n\sqrt{\Delta^2 + (\gamma_3|g_k| + \beta_n\gamma_1)^2}. \tag{18}$$

With the analytic wave functions in Eq. (16), Berry connections $\boldsymbol{\xi}_{nmk}$ can be calculated directly from Eq. (5), as listed in Appendix A, where the relations between all components are also presented. The selection rules for r^z_{nmk} are

$$r^z_{13k} = r^z_{31k} = \frac{c\mathcal{N}_{-1k}}{2}, \quad r^z_{24k} = r^z_{42k} = \frac{c\mathcal{N}_{+1k}}{2}. \tag{19}$$

Therefore, r^z_{nmk} is nonzero only for the band pair $(n, m) = (1, 3)$ or (2,4). The injection coefficient becomes

$$\eta^{xzx}(\omega) = \frac{e^3}{2\pi\hbar^2}\int d\boldsymbol{k}\{f_{13k}\mathcal{V}^x_{31k}\mathrm{Im}[r^x_{31k}r^z_{13k}]\delta(\omega_{31k} - \omega) + f_{24k}\mathcal{V}^x_{42k}\mathrm{Im}[r^x_{42k}r^z_{24k}]\delta(\omega_{42k} - \omega)\}. \tag{20}$$

The intraband Berry connections are obtained as

$$\boldsymbol{\xi}_{nnk} = \frac{1}{2}\left[g^*_k(i\boldsymbol{\nabla}_k)g_k + \frac{a_0}{\sqrt{3}}\hat{\boldsymbol{y}}\right] + \frac{1}{2}c\hat{\boldsymbol{z}}\left(1 + \alpha_n\sqrt{1 - \mathcal{N}^2_{\beta_n k}}\right). \tag{21}$$

The matrix elements for $\xi^{x/y}_{nnk}$ are independent of the band index n; thus, $(r^a_k)_{;nmk^b} = \frac{\partial r^a_{nmk}}{\partial k^b}$ for $b = x, y$, and $(r^a_k)_{;nmk^z} = -i(\xi^z_{nnk} - \xi^z_{mmk})r^a_{nmk}$. The shift conductivities become

$$\sigma^{xzx}(\omega) = -i\frac{e^3}{4\pi\hbar^2}\int d\boldsymbol{k}\left[f_{13k}\left(r^z_{31k}\frac{\partial r^x_{13k}}{\partial k_x} + r^x_{31k}\frac{\partial r^z_{13k}}{\partial k_x}\right)\delta(\omega_{31k} - \omega) + f_{24k}\left(r^z_{42k}\frac{\partial r^x_{24k}}{\partial k_x} + r^x_{42k}\frac{\partial r^z_{24k}}{\partial k_x}\right)\delta(\omega_{42k} - \omega)\right], \tag{22a}$$

$$\sigma^{zzz}(\omega) = \frac{e^3}{2\pi\hbar^2}\int d\boldsymbol{k}\left[f_{12k}\left|r^z_{31k}\right|^2(\xi^z_{33k} - \xi^z_{11k})\delta(\omega_{31k} - \omega) + f_{24k}\left|r^z_{42k}\right|^2(\xi^z_{44k} - \xi^z_{22k})\delta(\omega_{42k} - \omega)\right], \tag{22b}$$

$$\sigma^{zxx}(\omega) = \frac{e^3}{2\pi\hbar^2}\int d\boldsymbol{k}\sum_{nm} f_{nmk}\left|r^x_{mnk}\right|^2 \times(\xi^z_{mmk} - \xi^z_{nnk})\delta(\omega_{mnk} - \omega). \tag{22c}$$

It can be seen that the coefficients η^{xzx}, σ^{xzx}, and σ^{zzz} are induced by the transitions only from band 1 to 3 or from band 2 to 4, while σ^{zxx} has no such limit. These coefficients can be further simplified with the analytical expressions for all these quantities, which can be obtained under the linear dispersion approximation around the Dirac points, as shown in Appendix B.

Figure 2(a) shows the band structure of AA-BG for $\Delta = 0$ and 0.4 eV. With the application of a gate voltage, the interlayer coupling shifts the energies of the Dirac cones of each layer, while the electronic states at zero energy are still degenerate. Bands 1 and 3 (or 2 and 4) are approximately parallel to each other, and their energy differences are in the range of $2\sqrt{\Delta^2 + (\gamma_1 + 3\gamma_3)^2} \leqslant \hbar\omega_{42k} \leqslant 2\sqrt{\Delta^2 + \gamma_1^2} \leqslant \hbar\omega_{31k} \leqslant 2\sqrt{\Delta^2 + (\gamma_1 - 3\gamma_3)^2}$ because $0 \leqslant |g_k| \leqslant 3$, where the middle value is obtained at the Dirac points and the other two values are obtained at the M points. Figure 2(b) gives the joint densities of states (JDOSs) $\mathcal{J}_{31}(\omega)$ and $\mathcal{J}_{42}(\omega)$ for two related pairs of bands, which are defined as

$$\mathcal{J}_{nm}(\omega) = \int d\boldsymbol{k}\delta(\hbar\omega_{nmk} - \hbar\omega). \tag{23}$$

These two JDOSs are strongly localized in energy, regardless of whether there is a gate voltage. For $\Delta = 0.4$ eV, $\mathcal{J}_{42}(\omega)$ is nonzero in the energy range of [0.95, 1.08] eV, and $\mathcal{J}_{31}(\omega)$ is nonzero in the energy range of [1.08, 1.21] eV.

B. Band structure of AB-BG

The Hamiltonian in Eq. (2) for AB-BG can also be analytically diagonalized, as shown in Appendix C, but the expressions for the eigenenergies are too complicated to provide meaningful physical insight; thus, we discuss the band structure based on numerical calculation. This work focuses on the electronic transitions around the Dirac

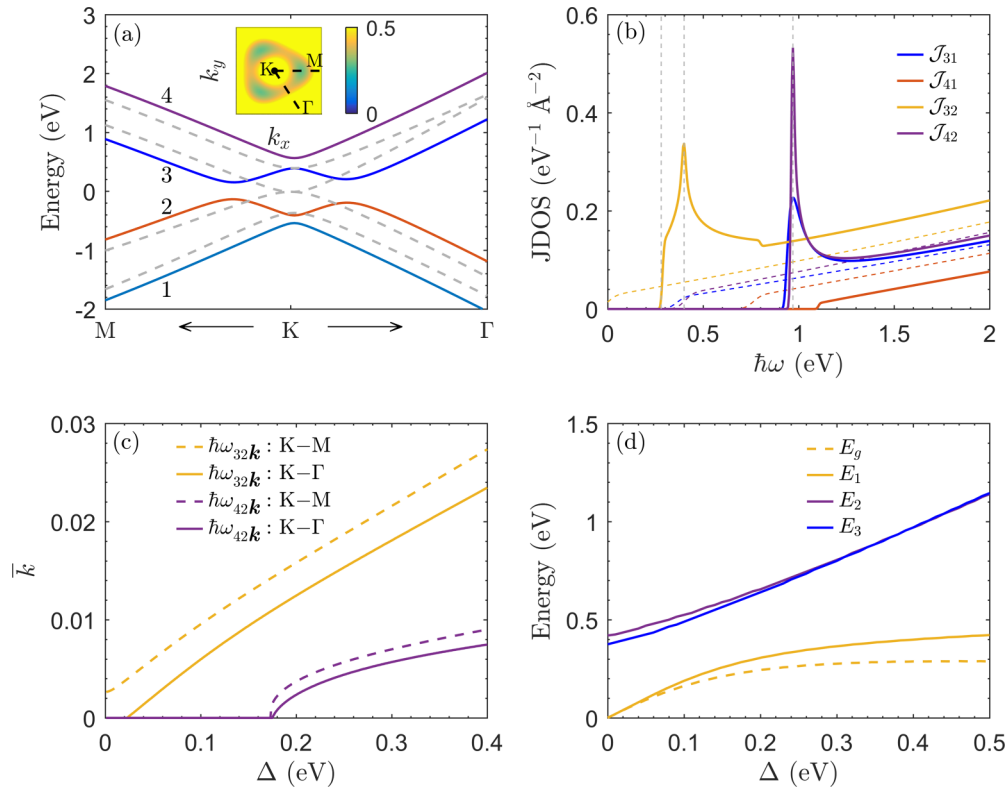

FIG. 3. (a) Band structure and (b) JDOS for AB-BG at $\Delta = 0$ (dashed curves) and $\Delta = 0.4$ eV (solid curves). The energetic locations of the band gap E_g and the maximal values of $\mathcal{J}_{32}$, $\mathcal{J}_{42}$, and $\mathcal{J}_{31}$ (E_1, E_2, E_3) are indicated. The inset shows the $\boldsymbol{k}$-resolved energy difference $\hbar\omega_{32\boldsymbol{k}}$ for $\Delta = 0.4$ eV. (c) Δ dependence of the $\boldsymbol{k}$ location for the minimum of $\hbar\omega_{nm\boldsymbol{k}}$ along the $K-M$ and K-Γ directions. (d) Δ dependence of E_g, E_1, E_2, and E_3.

points; for convenience, the wave vectors are expressed as $\boldsymbol{k} = \bar{k}\frac{2\pi}{a_0}(\hat{\boldsymbol{x}}\cos\theta + \hat{\boldsymbol{y}}\sin\theta) + \boldsymbol{K}$, with $\theta = 2n\pi/3$ along the K-M directions and $\theta = (2n+1)\pi/3$ along the K-Γ directions. Figure 3(a) gives the band structure for AB-BG at gate voltages $\Delta = 0$ and 0.4 eV. At $\Delta = 0$, in each Dirac cone, the two middle bands are degenerate at the Dirac points with $\bar{k} = 0$ and the other three $\boldsymbol{k}$ points on the K-M paths with $\bar{k} = -\frac{\gamma_1'\gamma_3'}{\sqrt{3}\pi\gamma_0'^2} \sim 0.003$ (see details in Appendix C). Meanwhile, the energy differences, $\hbar\omega_{31\boldsymbol{k}}$ and $\hbar\omega_{42\boldsymbol{k}}$, have minima at the Dirac points. For nonzero gate voltage, the degeneracy at these points is lifted. The eigenenergies at the Dirac points are $\pm\Delta - \frac{\Delta'}{2}$ and $\pm\sqrt{\Delta^2+\gamma_1^2} + \frac{\Delta'}{2}$, and the middle two bands around the Dirac points have a Mexican hat shape [43]. At $\Delta = 0.4$ eV, the energy difference $\hbar\omega_{32\boldsymbol{k}}$ shows a minimum with increasing $\bar{k}$ for each θ, as shown in the $\boldsymbol{k}$-resolved energy difference in the inset, where the threefold rotational symmetry can clearly be seen around this Dirac point. Along the K-M directions, the minima of $\hbar\omega_{32\boldsymbol{k}}$ appear around $\bar{k} = 0.027$ to give a band gap of $E_g = 0.28$ eV, and along the K-Γ directions, the minima appear around $\bar{k} = 0.023$, which have an energy $E_1 = 0.4$ eV higher than the band gap and give a van Hove singularity (VHS). Similar results can be found for $\hbar\omega_{42\boldsymbol{k}}$, and another VHS appears with energy $E_2 = 0.97$ eV; however, $\hbar\omega_{31\boldsymbol{k}}$ shows a minimum at the Dirac points, but no VHS appears. Figure 3(b) gives JDOSs of $\mathcal{J}_{31}(\omega)$, $\mathcal{J}_{32}(\omega)$, $\mathcal{J}_{41}(\omega)$, and $\mathcal{J}_{42}(\omega)$ at $\Delta = 0$ and 0.4 eV. The gate voltage changes these JDOSs significantly around the band edge. $\mathcal{J}_{32}(\omega)$ and $\mathcal{J}_{42}(\omega)$ have divergences at the VHS points with energies E_1 and E_2, respectively; $\mathcal{J}_{31}(\omega)$ has a peak located at $E_3 \sim 0.97$ eV around the band edge, which is induced by the nearly parallel bands (1, 3) around the Dirac points.

The VHS points do not appear for all gate voltages. Figure 3(c) exhibits Δ dependence of the $\bar{k}$ value for the minimal energy of $\hbar\omega_{32\boldsymbol{k}}$ and $\hbar\omega_{42\boldsymbol{k}}$ for θ along the K-M and K-Γ directions, respectively. Along the K-M directions, $\hbar\omega_{32\boldsymbol{k}}$ has a minimum value at nonzero $\bar{k}$ for all Δ, which gives the band gap E_g of the system; however, along the K-Γ directions, the minimum energy E_1 moves to a nonzero $\bar{k}$ only for $\Delta \geqslant 0.023$ eV, where a VHS appears as well. Note that the JDOS $\mathcal{J}_{32\boldsymbol{k}}$ shows a maximum at the band edge when there is no VHS for $\Delta < 0.023$ eV. However, the minima of $\hbar\omega_{42\boldsymbol{k}}$ along the K-M and K-Γ directions do not locate at the Dirac points only for $\Delta \geqslant 0.174$ eV, where a VHS appears as well. For $\Delta < 0.174$ eV, $\mathcal{J}_{42}(\omega)$ also shows a maximum at the band edge between bands 4 and 2, where this energy is still denoted E_2; the maximum of $\mathcal{J}_{31}(\omega)$ also locates at the band edge between bands 3 and 1, where this energy is still denoted E_3. The gate voltage dependences of these energies E_g, E_1, E_2, and E_3 are shown in Fig. 3(d).

C. Injection coefficients and shift conductivities at $\Delta = 0.4$ eV

In this section we present the numerical results for the injection coefficient $\eta^{xzx}(\omega)$ and shift conductivities $\sigma^{yyy}(\omega)$, $\sigma^{xzx}(\omega)$, $\sigma^{zxx}(\omega)$, and $\sigma^{zzz}(\omega)$. The parameters are chosen to

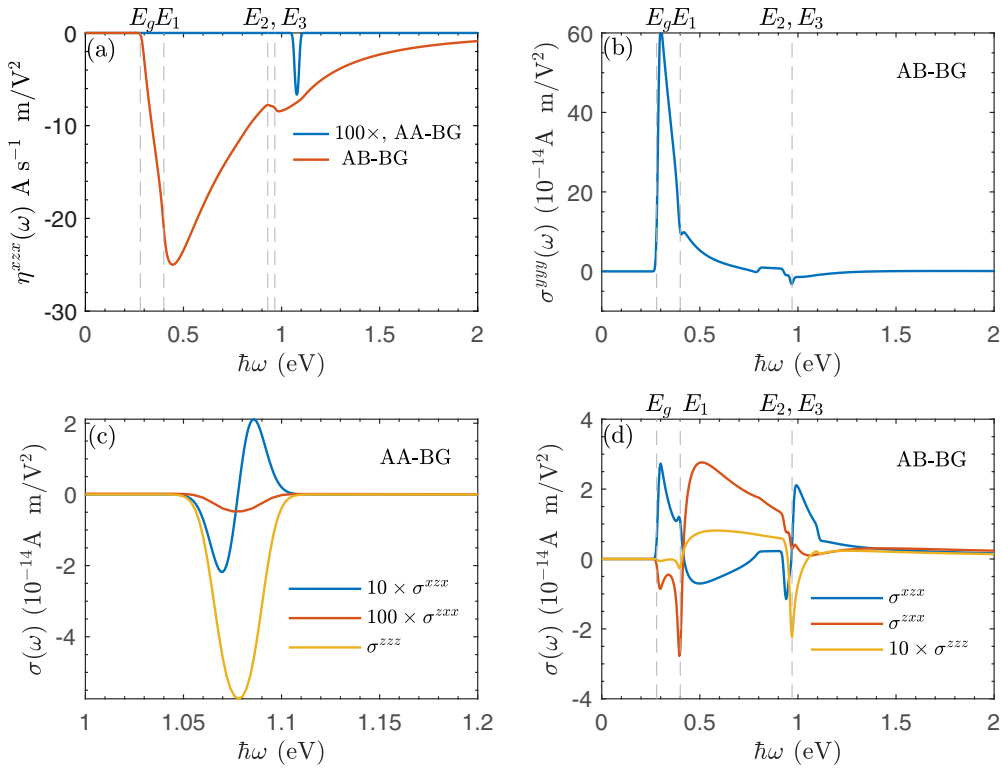

FIG. 4. Injection coefficients and shift conductivities for AA-BG and AB-BG at $\Delta = 0.4$ eV. (a) η^{xzx} for AA-BG and AB-BG, (b) σ^{yyy} for AB-BG, (c) σ^{xzx}, σ^{zxx}, and σ^{zzz} for AA-BG, and (d) σ^{xzx}, σ^{zxx}, and σ^{zzz} for AB-BG.

be $T = 300$ K, $\mu = 0$, and $\Delta = 0.4$ eV. During the numerical calculation, the Brillouin zone is divided into a 3000×3000 homogeneous grid. The δ functions in Eqs. (11) and (13) are approximated by a Gaussian function as $\delta(\omega) = \frac{\hbar}{\sqrt{\pi}\Gamma} e^{-(\hbar\omega)^2/\Gamma^2}$, with Gaussian broadening $\Gamma = 10$ meV.

Figure 4(a) shows the injection coefficient spectra for AA-BG and AB-BG. For the injection in AA-BG, the spectrum is just a peak located in a very narrow energy range, $1.069 < \hbar\omega < 1.087$ eV, with an absolute value of about 0.067 A s^{-1} m V^{-2}. From the analytic results shown in Eq. (B16), the spectra include two contributions in different photon energy regions: one is from the optical transition between bands 1 and 3 for photon energy $\hbar\omega > 2\sqrt{\Delta^2 + \gamma_1^2}$, or $1.078 < \hbar\omega < 1.087$ eV, and the other is between bands 2 and 4 for $\hbar\omega < 2\sqrt{\Delta^2 + \gamma_1^2}$, or $1.069 < \hbar\omega < 1.078$ eV; both magnitudes are nearly proportional to $\hbar\omega - 2\sqrt{\Delta^2 + \gamma_1^2}$. These two contributions merge as a single peak just because the δ function is numerically broadened with $\Gamma = 10$ meV, which is even larger than each energy region. The injection coefficient η^{xzx} in AB-BG starts with photon energy higher than the gap, i.e., $\hbar\omega > 0.28$ eV, and reaches its maximum value of 25 A s^{-1} m V^{-2} in amplitude at $\hbar\omega = 0.45$ eV, which is slightly larger than the first VHS energy of JDOS E_1; the energy difference arises from the zero electron velocity at this VHS. Considering the thickness of a bilayer graphene to be $2c = 6.7$ Å, the effective bulk injection coefficient is 3.7×10^{10} μA s^{-1} V^{-2}, which is nearly 50 times larger than that in bulk GaAs [44]. After this peak, the amplitude of the injection coefficient decreases as the photon energy increases, except for a small peak located around the JDOS peak at higher energy E_2 or E_3. It can be seen that the injection coefficient for AB-BG is about two orders of magnitude larger than that for AA-BG. This magnitude difference arises from three aspects: (1) Because the optical transition of AA-BG can occur only between the nearly parallel bands, the velocities of the conduction bands and the valence bands have the same signs and similar amplitudes, which leads to very small velocity differences $\mathcal{V}^x_{13}$ and $\mathcal{V}^x_{24\boldsymbol{k}}$. However, for AB-BG, they are opposite, and the value of $\mathcal{V}^x_{23}$ is about two orders of magnitude larger than that in AA-BG. (2) The JDOSs in AA-BG are about two orders of magnitude larger than those in AB-BG [see Figs. 2(b) and 3(b)]. (3) The optical transition amplitudes $\mathrm{Im}[r^x_{mn\boldsymbol{k}} r^z_{nm\boldsymbol{k}}]$ for AB-BG are about two orders of magnitude larger than those for AA-BG, and the difference mostly arises from the values of $r^x_{13\boldsymbol{k}}$ and $r^x_{24\boldsymbol{k}}$ for AA-BG and $r^x_{23\boldsymbol{k}}$ for AB-BG. This difference may arise from the fact that the gate voltage opens the gap in AB-BG, which induces a larger Berry connection, while it just shifts the Dirac cones in AA-BG, which makes $r^x_{13\boldsymbol{k}}$ and $r^x_{24\boldsymbol{k}}$ nearly proportional to the gate voltage [see Eqs. (A2a) and (A2b)]. Overall, the injection coefficients in AA-BG are about two orders of magnitude smaller than those in AB-BG. To have a direct effect on these values, we give an estimation of how large the injection current can be in AB-BG. Based on Eq. (14), when the laser is a 45° obliquely incident p-polarized light with photon energy of 0.45 eV, light intensity of $I = 0.1$ GW/cm^2, and pulse duration of $\tau = 1$ ps, the generated injection current is the difference of $2\eta^{xzx}\frac{I}{2c\epsilon_0} W\tau \sim 9$ mA for an electrode with a width $W = 1$ μm.

Then we turn to the shift conductivities, as shown in Figs. 4(b)–4(d). Figure 4(c) gives the shift conductivity for

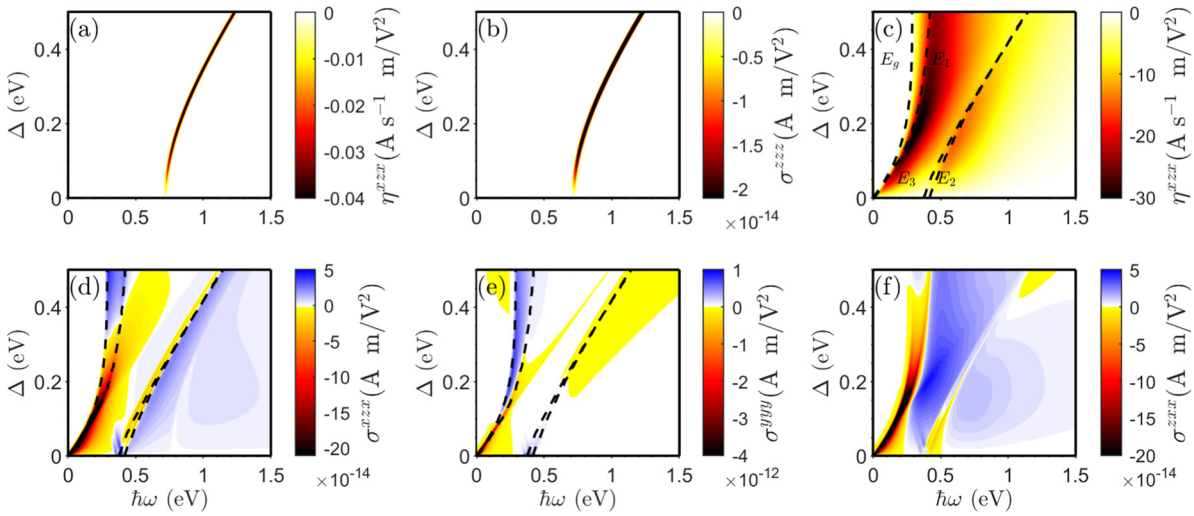

FIG. 5. Gate voltage dependence of injection coefficients and shift conductivities at zero chemical potential. (a) $\eta^{xzx}(\omega)$ and (b) $\sigma^{zzz}(\omega)$ for AA-BG and (c) $\eta^{xzx}(\omega)$, (d) $\sigma^{xzx}(\omega)$, (e) $\sigma^{yyy}(\omega)$, and (f) $\sigma^{zxx}(\omega)$ for AB-BG. In (c)–(f), dashed curves indicate the characteristic energies E_g, E_1, E_2, and E_3 for AB-BG.

AA-BG. It can be seen that the component σ^{zzz} is about one order of magnitude larger than σ^{xzx} or is at least two orders of magnitude larger than σ^{zxx}. Both σ^{zzz} and σ^{xzx} have nonzero values only in the very narrow energy regions, similar to the injection coefficient. These results are consistent with the analytic results shown in Eqs. (B17) and (B18). Interestingly, σ^{xzx} includes the contributions from band 1 to 3 and from band 2 to 4, but with opposite signs. For AB-BG shown in Figs. 4(b) and 4(d), all nonzero components start from the band edge $\hbar\omega \geqslant E_g$. Different from the injection coefficients, the shift conductivities at the band edge are nonzero and show prominent peaks. Especially, σ^{yyy} shows a large value of about 6×10^{-13} A m V^{-2} at the band edge, and it drops quickly with increasing photon energy. The effective bulk shift conductivity is 896 μA/V^2, which is several times larger than in GeSe (200 μA/V^2) [44]. In addition, the component σ^{zzz} is at least one order of magnitude smaller than other nonzero components, totally different from the case of AA-BG, where it is the largest one. The spectra of σ^{xzx} and σ^{zxx} have similar amplitudes around 2×10^{-14} A m V^{-2}, which is tens of times smaller than the peak of σ^{yyy}; they also show some fine structures around the characteristic energies E_1, E_2, and E_3. For these common components of shift conductivities for two types of bilayer graphene, the values of σ^{xzx} and σ^{zxx} for AB-BG are about 10 and 100 times larger than those of AA-BG, respectively, while the value of σ^{zzz} for AB-BG is smaller. We repeat the above estimation for the shift current using the same parameters but $\hbar\omega = 0.3$ eV and then obtain the generated shift current of $2\sigma^{yyy}\frac{I}{2c\epsilon_0}W \sim 0.23$ mA.

D. Effects of gate voltage

Figure 5 gives the gate voltage dependence of the injection coefficients and shift conductivities for AA-BG and AB-BG at zero chemical potential. Note that the negative gate voltage leads to opposite coefficients, which are consistent with the results by Xiong *et al.* [33]; thus, only positive gate voltages are shown here.

Figures 5(a) and 5(b) show the spectra of η^{xzx} and σ^{zzz} for AA-BG, respectively. As indicated in the previous section, both spectra for different gate voltages are nonzero in a very narrow photon energy region. With an increase in the gate voltage, the region moves to larger energy, and the values of both spectra increase, as indicated by $\propto\Delta$ in Eqs. (B20) and (B22). Figure 5(c) gives the injection coefficient η^{xzx} for AB-BG. At each gate voltage, the injection coefficient shows two peaks located at photon energies slightly larger than E_1 and E_2, which were discussed in the previous section. As the gate voltage Δ varies, the peak amplitude reaches a maximum at $\Delta \sim 0.2$ eV. The shift conductivities σ^{xzx}, σ^{yyy}, and σ^{zxx} for AB-BG are plotted in Figs. 5(d)–5(f). They show some similar characteristics: (1) The spectra are located at about the band gap, similar to what happens in the case of $\Delta = 0.4$ eV, and their amplitudes increase with the decrease of Δ; σ^{xzx} and σ^{zxx} increase much faster than σ^{yyy}. (2) Sign changes of shift conductivities exist.

E. Effects of the chemical potential

The chemical potential μ dependence of the injection coefficients and shift conductivities at $\Delta = 0.4$ eV are depicted in Fig. 6 using the same layout as in Fig. 5. For AA-BG in Figs. 6(a) and 6(b), they show very similar asymmetric dependence on the chemical potential: with the increase of the chemical potential, the values of all coefficients increase, and the locations shift to higher or lower photon energies depending on the sign of the chemical potential. For positive chemical potential, the transitions between bands 1 and 3 are suppressed according to the Pauli blocking effects, while new extra transitions between bands 2 and 4 appear due to the additional free electrons in band 2. The extra transitions require lower photon energy and redshift the spectra, and they also correspond to larger JDOSs, leading to larger coefficients. Similar results can be found for negative chemical potential, but with the band pairs (1, 2) and (3, 4) switched.

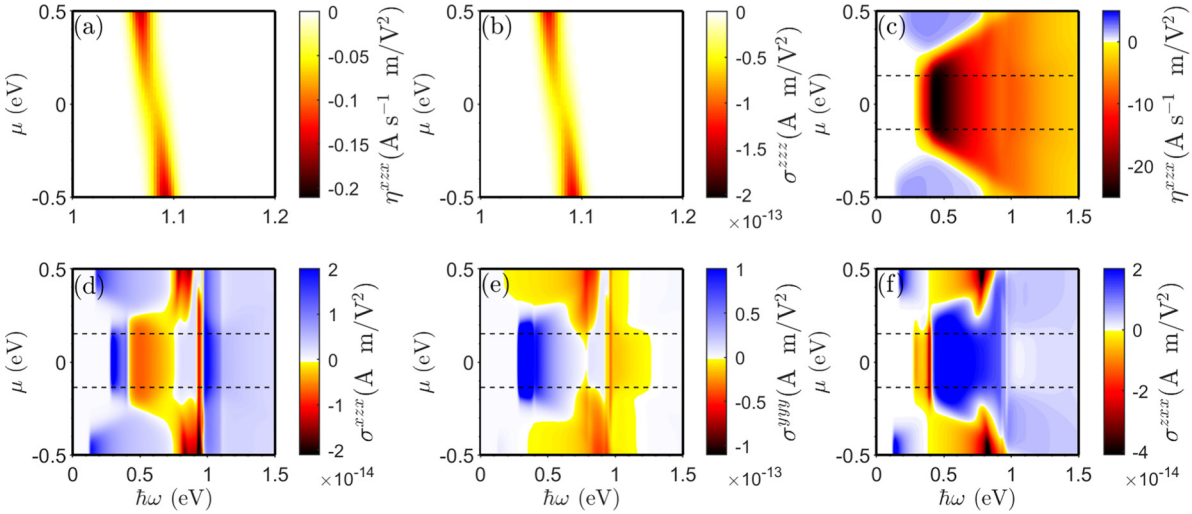

FIG. 6. Chemical potential dependence of injection coefficients and shift conductivities at $\Delta = 0.4$ eV. (a) $\eta^{xzx}(\omega)$ and (b) $\sigma^{zzz}(\omega)$ for AA-BG and (c) $\eta^{xzx}(\omega)$, (d) $\sigma^{xzx}(\omega)$, (e) $\sigma^{yyy}(\omega)$, and (f) $\sigma^{zxx}(\omega)$ for AB-BG. The dashed lines in (c)–(f) indicate the position of the conduction and valence band edges for AB-BG.

In AB-BG, the chemical potential μ has different effects, as shown in Figs. 6(c)–6(f). Due to the existence of the band gap, the spectra barely change when the chemical potential lies in the gap. When μ is above the conduction band edge or below the valence band edge, the main peak of η^{xzx} around 0.5 eV is reduced gradually due to the Pauli blocking, and new transitions appear between bands 1 and 2 or 3 and 4 to give additional injections with opposite signs. Similar results are obtained for the shift conductivities.

IV. CONCLUSION

In this paper we have studied gate voltage induced injection current and shift current in AA- and AB-stacked bilayer graphene. The gate voltage plays a crucial role in breaking the inversion symmetry of bilayer graphene to induce photogalvanic effects. In AA-BG, the injection and shift currents are mainly induced by optical transitions between two pairs of nearly parallel bands; the coefficient spectra locate in a very narrow photon energy region of about 20 meV. In AB-BG, the gate voltage effectively changes the band structure for AB-BG with gap openings located in the K-M directions and additional VHSs located in the K-Γ directions. The optical transition can occur between any possible band pairs, and the structures of spectra are strongly determined by the band gap and the VHS energies. For both stacking orders, the injection and shift currents can be generated by the existence of an oblique p-polarized light component, while the in-plane shift currents in AB-BG can also be generated by normal incident light. The out-of-plane shift current finally results in a static electric polarization between layers. The stacking order has significant effects on both currents. The injection coefficient for AA-BG is about two orders of magnitude smaller than that for AB-BG; for the shift conductivities, besides the additional components σ^{yyy} that appear in AB-BG that are one order of magnitude larger than other components, the components σ^{xzx} and σ^{zxx} of AB-BG are one or two orders of magnitude larger than those of AA-BG, while σ^{zzz} is one order of magnitude smaller. This significant difference can be used to distinguish the stacking order by accurately measuring the tensor components in experiment, especially the component σ^{yyy}. All these coefficients can be effectively modulated by the gate voltage and the chemical potential. Our results suggest that gate voltage controlled bilayer graphene can be used to realize tunable optoelectronic detectors working in the midinfrared.

ACKNOWLEDGMENTS

This work was supported by National Natural Science Foundation of China Grants No. 12034003, No. 12004379, and No. 62250065. J.L.C. acknowledges the support from the Talent Program of CIOMP.

APPENDIX A: BERRY CONNECTIONS OF AA-BG

The general expression for the Berry connection of AA-BG is

$$\begin{aligned}\boldsymbol{\xi}_{nm\boldsymbol{k}} = &(\sqrt{1-\alpha_n\mathcal{N}_{\beta_n\boldsymbol{k}}}\sqrt{1-\alpha_m\mathcal{N}_{\beta_m\boldsymbol{k}}}+\alpha_n\alpha_m\sqrt{1+\alpha_n\mathcal{N}_{\beta_n\boldsymbol{k}}}\sqrt{1+\alpha_m\mathcal{N}_{\beta_m\boldsymbol{k}}})\frac{1+\beta_n\beta_m}{8}[\hat{g}^*_{\boldsymbol{k}}(i\nabla_{\boldsymbol{k}}\hat{g}_{\boldsymbol{k}})+\hat{\boldsymbol{y}}d]\\ &+(\alpha_m\sqrt{1-\alpha_n\mathcal{N}_{\beta_n\boldsymbol{k}}}\sqrt{1+\alpha_m\mathcal{N}_{\beta_m\boldsymbol{k}}}+\alpha_n\sqrt{1+\alpha_n\mathcal{N}_{\beta_n\boldsymbol{k}}}\sqrt{1-\alpha_m\mathcal{N}_{\beta_m\boldsymbol{k}}})\\ &\times\frac{\beta_n\beta_m-1}{8}[\hat{g}^*_{\boldsymbol{k}}(i\nabla_{\boldsymbol{k}}\hat{g}_{\boldsymbol{k}})-\hat{\boldsymbol{y}}d]\end{aligned}$$

$$+\frac{i\delta_{\beta_n\beta_m}}{2}(\sqrt{1-\alpha_n\mathcal{N}_{\beta_n\boldsymbol{k}}}\nabla_{\boldsymbol{k}}\sqrt{1-\alpha_m\mathcal{N}_{\beta_m\boldsymbol{k}}}+\alpha_n\alpha_m\sqrt{1+\alpha_n\mathcal{N}_{\beta_n\boldsymbol{k}}}\nabla_{\boldsymbol{k}}\sqrt{1+\alpha_m\mathcal{N}_{\beta_m\boldsymbol{k}}})$$
$$+(\sqrt{1-\alpha_n\mathcal{N}_{\beta_n\boldsymbol{k}}}+\alpha_n\sqrt{1+\alpha_n\mathcal{N}_{\beta_n\boldsymbol{k}}})(\sqrt{1-\alpha_m\mathcal{N}_{\beta_m\boldsymbol{k}}}+\alpha_m\sqrt{1+\alpha_m\mathcal{N}_{\beta_m\boldsymbol{k}}})\frac{1+\beta_n\beta_m}{8}c\hat{\boldsymbol{z}}, \tag{A1}$$

with $d=\sqrt{3}/3a_0$. Here we give the x component between different bands as

$$r^x_{13\boldsymbol{k}}=-r^x_{31\boldsymbol{k}}=-\frac{i}{2}\frac{\frac{\partial\mathcal{N}_{-1\boldsymbol{k}}}{\partial k_x}}{\sqrt{1-\mathcal{N}^2_{-1\boldsymbol{k}}}}=-\frac{i}{2}\frac{\gamma_3}{|\Delta|}(1-\mathcal{N}^2_{-1\boldsymbol{k}})\frac{\partial|g_{\boldsymbol{k}}|}{\partial k_x}, \tag{A2a}$$

$$r^x_{24\boldsymbol{k}}=-r^x_{42\boldsymbol{k}}=-\frac{i}{2}\frac{\frac{\partial\mathcal{N}_{+1\boldsymbol{k}}}{\partial k_x}}{\sqrt{1-\mathcal{N}^2_{+1\boldsymbol{k}}}}=-\frac{i}{2}\frac{\gamma_3}{|\Delta|}(1-\mathcal{N}^2_{+1\boldsymbol{k}})\frac{\partial|g_{\boldsymbol{k}}|}{\partial k_x}, \tag{A2b}$$

$$r^x_{12\boldsymbol{k}}=r^x_{21\boldsymbol{k}}=-r^x_{34\boldsymbol{k}}=-r^x_{43\boldsymbol{k}}=\frac{1}{4}[\sqrt{1+\mathcal{N}_{-1\boldsymbol{k}}}\sqrt{1-\mathcal{N}_{+1\boldsymbol{k}}}+\sqrt{1-\mathcal{N}_{-1\boldsymbol{k}}}\sqrt{1+\mathcal{N}_{+1\boldsymbol{k}}}]\left[\hat{g}^*_{\boldsymbol{k}}\left(i\frac{\partial\hat{g}_{\boldsymbol{k}}}{\partial k_x}\right)\right], \tag{A2c}$$

$$r^x_{32\boldsymbol{k}}=-r^x_{23\boldsymbol{k}}=r^x_{14\boldsymbol{k}}=-r^x_{41\boldsymbol{k}}=\frac{1}{4}[\sqrt{1+\mathcal{N}_{-1\boldsymbol{k}}}\sqrt{1-\mathcal{N}_{+1\boldsymbol{k}}}-\sqrt{1-\mathcal{N}_{-1\boldsymbol{k}}}\sqrt{1+\mathcal{N}_{+1\boldsymbol{k}}}]\left[\hat{g}^*_{\boldsymbol{k}}\left(i\frac{\partial\hat{g}_{\boldsymbol{k}}}{\partial k_x}\right)\right]. \tag{A2d}$$

Combined with other quantities in Eqs. (19) and (21), the injection coefficients and the shift conductivities can be evaluated. For the latter use, we also need

$$\mathcal{V}_{21\boldsymbol{k}}=\frac{2\gamma_3}{\hbar}\mathcal{N}_{-1\boldsymbol{k}}\frac{\partial|g_{\boldsymbol{k}}|}{\partial k_x}, \tag{A3}$$

$$\mathcal{V}_{43\boldsymbol{k}}=\frac{2\gamma_3}{\hbar}\mathcal{N}_{+1\boldsymbol{k}}\frac{\partial|g_{\boldsymbol{k}}|}{\partial k_x}. \tag{A4}$$

APPENDIX B: ANALYTICAL EXPRESSIONS FOR η^{xzx}, σ^{xzx}, AND σ^{zzz} IN AA-BG UNDER THE LINEAR DISPERSION APPROXIMATION

Here we give the analytic results for η^{xzx} in Eq. (20), σ^{xzx} in Eq. (22a), and σ^{zzz} in Eq. (22b) under the linear dispersion approximation around the Dirac points. The term σ^{zxx} is not discussed due to its very small magnitude, as shown in Fig. 4(c).

The integrands of η^{xzx}, σ^{xzx}, and σ^{zzz} are functions of $|g_{\boldsymbol{k}}|$, $\frac{\partial|g_{\boldsymbol{k}}|}{\partial k_x}$, and $\frac{\partial^2|g_{\boldsymbol{k}}|}{\partial k_x^2}$, where all terms involving $|g_{\boldsymbol{k}}|$ can be simplified by using the properties of the δ function. The function $\delta(\hbar\omega_{nm\boldsymbol{k}}-\hbar\omega)$ is nonzero only for $|g_{\boldsymbol{k}}|=G_{nm}$, with

$$\gamma_3 G_{31}=\gamma_1-\sqrt{\left(\frac{\hbar\omega}{2}\right)^2-\Delta^2},\quad \hbar\omega\geqslant 2\sqrt{\Delta^2+\gamma_1^2}, \tag{B1}$$

$$\gamma_3 G_{42}=\sqrt{\left(\frac{\hbar\omega}{2}\right)^2-\Delta^2}-\gamma_1,\quad \hbar\omega\leqslant 2\sqrt{\Delta^2+\gamma_1^2}. \tag{B2}$$

Further, we get

$$(\mathcal{N}_{-1\boldsymbol{k}})|_{|g_{\boldsymbol{k}}|=G_{31}}=-(\mathcal{N}_{+1\boldsymbol{k}})|_{|g_{\boldsymbol{k}}|=G_{42}}=-\sqrt{1-\left(\frac{2\Delta}{\hbar\omega}\right)^2}. \tag{B3}$$

(1) By substituting the expressions for $\mathcal{V}^x_{nm\boldsymbol{k}}$, $r^x_{31\boldsymbol{k}}$, $r^z_{13\boldsymbol{k}}$, $r^x_{42\boldsymbol{k}}$, and $r^z_{24\boldsymbol{k}}$, η^{xzx} becomes

$$\eta^{xzx}=\frac{e^3}{2\pi\hbar^2}\int d\boldsymbol{k}\left(\frac{c\gamma_3^2}{2\hbar|\Delta|}\right)\left\{f_{12\boldsymbol{k}}\mathcal{N}^2_{-1\boldsymbol{k}}(1-\mathcal{N}^2_{-1\boldsymbol{k}})\left(\frac{\partial|g_{\boldsymbol{k}}|}{\partial k_x}\right)^2\delta(\omega_{31\boldsymbol{k}}-\omega)+f_{34\boldsymbol{k}}\mathcal{N}^2_{+1\boldsymbol{k}}(1-\mathcal{N}^2_{+1\boldsymbol{k}})\left(\frac{\partial|g_{\boldsymbol{k}}|}{\partial k_x}\right)^2\delta(\omega_{42\boldsymbol{k}}-\omega)\right\}$$
$$=\frac{e^3c|\Delta|}{\pi\hbar^2(\hbar\omega)^2}\left[1-\left(\frac{2\Delta}{\hbar\omega}\right)^2\right]\{f_{13\boldsymbol{k}}|_{|g_{\boldsymbol{k}}|=G_{31}}\mathcal{F}_{31}(\omega)+f_{24\boldsymbol{k}}|_{|g_{\boldsymbol{k}}|=G_{42}}\mathcal{F}_{42}(\omega)\}, \tag{B4}$$

with

$$\mathcal{F}_{nm}(\omega)=\int d\boldsymbol{k}\left(\gamma_3\frac{\partial|g_{\boldsymbol{k}}|}{\partial k_x}\right)^2\delta(\hbar\omega_{nm\boldsymbol{k}}-\hbar\omega). \tag{B5}$$

(2) To get the result for σ^{xzx}, we use

$$\frac{\partial \mathcal{N}_{-1\boldsymbol{k}}}{\partial k_x} = \left(1-\mathcal{N}_{-1\boldsymbol{k}}^2\right)^{3/2}\frac{\gamma_3}{|\Delta|}\frac{\partial |g_{\boldsymbol{k}}|}{\partial k_x} \tag{B6}$$

to get

$$r_{31\boldsymbol{k}}^z\frac{\partial r_{13\boldsymbol{k}}^x}{\partial k_x}+r_{31\boldsymbol{k}}^x\frac{\partial r_{13\boldsymbol{k}}^z}{\partial k_x} = \frac{ic}{4}\left(1+\mathcal{N}_{-1\boldsymbol{k}}^2\right)\left(1-\mathcal{N}_{-1\boldsymbol{k}}^2\right)^{3/2}\left(\frac{\gamma_3}{|\Delta|}\frac{\partial |g_{\boldsymbol{k}}|}{\partial k_x}\right)^2-\frac{ic}{4}\mathcal{N}_{-1\boldsymbol{k}}\left(1-\mathcal{N}_{-1\boldsymbol{k}}^2\right)\frac{\gamma_3}{|\Delta|}\frac{\partial^2 |g_{\boldsymbol{k}}|}{\partial k_x^2}. \tag{B7}$$

Similar expressions can be obtained for terms involving $\boldsymbol{r}_{32\boldsymbol{k}}$. Then we get

$$\begin{aligned}\sigma^{xzx} = \frac{e^3c}{4\pi\hbar(\hbar\omega)^2}\Bigg\{&\left[2-\left(\frac{2\Delta}{\hbar\omega}\right)^2\right]\frac{2|\Delta|}{\hbar\omega}\left[f_{13\boldsymbol{k}}|_{|g_{\boldsymbol{k}}|=G_{31}}\mathcal{F}_{31}(\omega)+f_{24\boldsymbol{k}}|_{|g_{\boldsymbol{k}}|=G_{42}}\mathcal{F}_{42}(\omega)\right]\\ &-|\Delta|\sqrt{1-\left(\frac{2\Delta}{\hbar\omega}\right)^2}\left[f_{13\boldsymbol{k}}|_{|g_{\boldsymbol{k}}|=G_{31}}\mathcal{Q}_{31}(\omega)-f_{24\boldsymbol{k}}|_{|g_{\boldsymbol{k}}|=G_{42}}\mathcal{Q}_{42}(\omega)\right]\Bigg\},\end{aligned} \tag{B8}$$

with

$$\mathcal{Q}_{nm}(\omega) = \int d\boldsymbol{k}\gamma_3\frac{\partial^2|g_{\boldsymbol{k}}|}{\partial k_x^2}\delta(\hbar\omega_{nm\boldsymbol{k}}-\hbar\omega). \tag{B9}$$

(3) The term $\sigma^{zzz}(\omega)$ becomes

$$\begin{aligned}\sigma^{zzz}(\omega) &= \frac{e^3}{2\pi\hbar^2}\int d\boldsymbol{k}\left\{f_{13\boldsymbol{k}}\frac{c^2}{4}\mathcal{N}_{-1\boldsymbol{k}}^2c\sqrt{1-\mathcal{N}_{-1\boldsymbol{k}}^2}\delta(\omega_{31\boldsymbol{k}}-\omega)+f_{24\boldsymbol{k}}\frac{c^2}{4}\mathcal{N}_{+1\boldsymbol{k}}^2c\sqrt{1-\mathcal{N}_{+1\boldsymbol{k}}^2}\delta(\omega_{42\boldsymbol{k}}-\omega)\right\}\\ &= \frac{e^3c^3}{4\pi\hbar}\frac{|\Delta|}{\hbar\omega}\left[1-\left(\frac{2\Delta}{\hbar\omega}\right)^2\right]\left[f_{13\boldsymbol{k}}|_{|g_{\boldsymbol{k}}|=G_{31}}\mathcal{J}_{31}(\omega)+f_{24\boldsymbol{k}}|_{|g_{\boldsymbol{k}}|=G_{42}}\mathcal{J}_{42}(\omega)\right].\end{aligned} \tag{B10}$$

When the optical transition occurs just around the Dirac points $\boldsymbol{K}$, we can approximate $|g_{\boldsymbol{k}+\boldsymbol{K}}| = \sqrt{3}a_0k/2$; then the δ functions can be worked out as

$$\delta[2\sqrt{\Delta^2+(\gamma_3|g_{\boldsymbol{k}}|-\gamma_1)^2}-\hbar\omega] = \frac{\delta[k-2G_{31}/(\sqrt{3}a_0)]}{\sqrt{3}a_0|\gamma_3|\sqrt{1-\left(\frac{2\Delta}{\hbar\omega}\right)^2}}\theta\left(\hbar\omega-2\sqrt{\Delta^2+\gamma_1^2}\right), \tag{B11}$$

$$\delta[2\sqrt{\Delta^2+(\gamma_3|g_{\boldsymbol{k}}|+\gamma_1)^2}-\hbar\omega] = \frac{\delta[k-2G_{42}/(\sqrt{3}a_0)]}{\sqrt{3}a_0|\gamma_3|\sqrt{1-\left(\frac{2\Delta}{\hbar\omega}\right)^2}}\theta\left(2\sqrt{\Delta^2+\gamma_1^2}-\hbar\omega\right). \tag{B12}$$

Then we get

$$\begin{pmatrix}\mathcal{J}_{31}(\omega)\\ \mathcal{J}_{42}(\omega)\end{pmatrix} = \frac{8\pi}{3a_0^2\gamma_3^2\sqrt{1-\left(\frac{2\Delta}{\hbar\omega}\right)^2}}\left|\gamma_1-\sqrt{\left(\frac{\hbar\omega}{2}\right)^2-\Delta^2}\right|\begin{pmatrix}\theta(\hbar\omega-2\sqrt{\Delta^2+\gamma_1^2})\\ \theta(2\sqrt{\Delta^2+\gamma_1^2}-\hbar\omega)\end{pmatrix}, \tag{B13}$$

$$\begin{pmatrix}\mathcal{F}_{31}(\omega)\\ \mathcal{F}_{42}(\omega)\end{pmatrix} = \frac{3a_0^2\gamma_3^2}{8}\begin{pmatrix}\mathcal{J}_{31}(\omega)\\ \mathcal{J}_{42}(\omega)\end{pmatrix}, \tag{B14}$$

$$\begin{pmatrix}\mathcal{Q}_{31}(\omega)\\ \mathcal{Q}_{42}(\omega)\end{pmatrix} = -\frac{\pi}{\sqrt{1-\left(\frac{2\Delta}{\hbar\omega}\right)^2}}\begin{pmatrix}\theta(\hbar\omega-2\sqrt{\Delta^2+\gamma_1^2})\\ \theta(2\sqrt{\Delta^2+\gamma_1^2}-\hbar\omega)\end{pmatrix}, \tag{B15}$$

where two Dirac points have been counted in the integration. In this approximation, the expressions for η^{xzx}, σ^{xzx}, and σ^{zzz} are

$$\eta^{xzx}(\omega) = \frac{e^3c|\Delta|\sqrt{1-\left(\frac{2\Delta}{\hbar\omega}\right)^2}}{\hbar^2(\hbar\omega)^2}\left|\gamma_1-\sqrt{\left(\frac{\hbar\omega}{2}\right)^2-\Delta^2}\right|[\mathcal{M}_{31}(\omega)+\mathcal{M}_{42}(\omega)], \tag{B16}$$

$$\sigma^{xzx}(\omega) = \frac{e^3c|\Delta|(\hbar^2\omega^2-2\Delta^2)}{2\hbar(\hbar\omega)^4\sqrt{1-\left(\frac{2\Delta}{\hbar\omega}\right)^2}}\left|\sqrt{1-\left(\frac{2\Delta}{\hbar\omega}\right)^2}-\frac{2\gamma_1}{\hbar\omega}\right|[\mathcal{M}_{31}(\omega)+\mathcal{M}_{42}(\omega)]-\frac{ce^3|\Delta|}{4\hbar(\hbar\omega)^2}(\mathcal{M}_{31}(\omega)-\mathcal{M}_{42}(\omega)), \tag{B17}$$

$$\sigma^{zzz}(\omega)=\frac{e^3c^3|\Delta|\sqrt{1-\left(\frac{2\Delta}{\hbar\omega}\right)^2}}{3\hbar(a_0\gamma_3)^2}\left|\sqrt{1-\left(\frac{2\Delta}{\hbar\omega}\right)^2}-\frac{2\gamma_1}{\hbar\omega}\right|[\mathcal{M}_{31}(\omega)+\mathcal{M}_{42}(\omega)], \tag{B18}$$

respectively, with

$$\begin{pmatrix}\mathcal{M}_{31}(\omega)\\ \mathcal{M}_{42}(\omega)\end{pmatrix}=\begin{pmatrix}f_{13\boldsymbol{k}}|_{|g_{\boldsymbol{k}}|=G_{31}}\theta\left(\hbar\omega-2\sqrt{\Delta^2+\gamma_1^2}\right)\\ f_{24\boldsymbol{k}}|_{|g_{\boldsymbol{k}}|=G_{42}}\theta\left(2\sqrt{\Delta^2+\gamma_1^2}-\hbar\omega\right)\end{pmatrix}. \tag{B19}$$

Through the Taylor expansion, the above expressions around frequency $2\sqrt{\Delta^2+\gamma_1^2}$ can be approximated as

$$\eta^{xzx}(\omega)\approx\frac{ce^3|\Delta||2\sqrt{\gamma_1^2+\Delta^2}-\hbar\omega|}{8\hbar^2\left(\gamma_1^2+\Delta^2\right)}[\mathcal{M}_{31}(\omega)+\mathcal{M}_{42}(\omega)], \tag{B20}$$

$$\sigma^{xzx}(\omega)\approx\frac{ce^3|\Delta|\left(2\gamma_1^2+\Delta^2\right)\left|2\sqrt{\gamma_1^2+\Delta^2}-\hbar\omega\right|}{32\hbar\gamma_1^2\sqrt{\gamma_1^2+\Delta^2}^3}[\mathcal{M}_{31}(\omega)+\mathcal{M}_{42}(\omega)]-\frac{ce^3|\Delta|}{16\hbar\left(\gamma_1^2+\Delta^2\right)}[\mathcal{M}_{31}(\omega)-\mathcal{M}_{42}(\omega)], \tag{B21}$$

$$\sigma^{zzz}(\omega)\approx\frac{ce^3|\Delta|\left|2\sqrt{\gamma_1^2+\Delta^2}-\hbar\omega\right|}{6\hbar a_0^2\gamma_3^2\left(\gamma_1^2+\Delta^2\right)}[\mathcal{M}_{31}(\omega)+\mathcal{M}_{42}(\omega)]. \tag{B22}$$

APPENDIX C: EIGENENERGIES OF AB-BG

The eigenenergies ϵ satisfy the equation

$$\left|H_{\boldsymbol{k}}^{\mathrm{AB}}-\epsilon\right|=0, \tag{C1}$$

or

$$\epsilon^4+x_2\epsilon^2+x_1\epsilon+x_0=0, \tag{C2}$$

with

$$x_2=-\gamma_1'^2-\left(2\gamma_0'^2+\gamma_3'^2+2\gamma_4'^2\right)|g_{\boldsymbol{k}}|^2-2\left[\Delta^2+\left(\frac{\Delta'}{2}\right)^2\right], \tag{C3}$$

$$x_1=-4\gamma_0'\gamma_4'\left(\gamma_1'|g_{\boldsymbol{k}}|^2+\gamma_3'\mathrm{Re}\left[g_{\boldsymbol{k}}^3\right]\right)+\Delta'\left(\gamma_3'^2|g_{\boldsymbol{k}}|^2-\gamma_1'^2\right), \tag{C4}$$

$$\begin{aligned}x_0=&\left(\gamma_0'^2-\gamma_4'^2\right)^2|g_{\boldsymbol{k}}|^4-2\gamma_3'\left[\gamma_1'\left(\gamma_0'^2+\gamma_4'^2\right)-\gamma_0'\gamma_4'\Delta'\right]\mathrm{Re}\left[g_{\boldsymbol{k}}^3\right]\\&+\left\{\gamma_3'^2\left[\gamma_1'^2+\Delta^2-\left(\frac{\Delta'}{2}\right)^2\right]-\left(2\gamma_0'^2-\gamma_3'^2\right)\left[\Delta^2-\left(\frac{\Delta'}{2}\right)^2\right]-2\gamma_0'\gamma_1'\gamma_4'\Delta'\right\}|g_{\boldsymbol{k}}|^2\\&+\left[\Delta^2-\left(\frac{\Delta'}{2}\right)^2\right]\left[\gamma_1'^2+\Delta^2-\left(\frac{\Delta'}{2}\right)^2\right].\end{aligned} \tag{C5}$$

Then the analytic expressions for the eigenenergies are

$$\epsilon_{n\boldsymbol{k}}=\frac{1}{2}\left[\alpha_n\sqrt{-2x_2-\beta_n\frac{2x_1}{\sqrt{y}}-y}+\beta_n\sqrt{y}\right],\quad n=1,2,3,4, \tag{C6}$$

with

$$y=\frac{1}{6}\left[4^{\frac{1}{3}}\left(y_1+\sqrt{y_1^2-4y_2^3}\right)^{\frac{1}{3}}+\frac{4^{\frac{2}{3}}y_2}{\left(y_1+\sqrt{y_1^2-4y_2^3}\right)^{\frac{1}{3}}}-4x_2\right], \tag{C7}$$

$$y_1=2x_2^3+27x_1^2-72x_2x_0, \tag{C8}$$

$$y_2=x_2^2+12x_0. \tag{C9}$$

At the Dirac points with $g_{\boldsymbol{k}}=0$, the four eigenenergies are $\pm\Delta-\frac{\Delta'}{2}$, $\pm\sqrt{\Delta^2+\gamma_1^2}+\frac{\Delta'}{2}$.

In general the electron-hole symmetry for AB-BG is broken due to the nonzero values of γ_4' and Δ'. However, we find that γ_4' and Δ' have negligible effects on the optical transition between bands 2 and 3. By setting $\gamma_4' = 0$ and $\Delta' = 0$, the eigenvalues become

$$\epsilon_{n\boldsymbol{k}} = \alpha_n \frac{1}{\sqrt{2}} \sqrt{z_1 + \alpha_n \beta_n \sqrt{z_2}}, \tag{C10}$$

with

$$z_1 = \gamma_1'^2 + 2\Delta^2 + \left(2\gamma_0'^2 + \gamma_3'^2\right)|g_{\boldsymbol{k}}|^2, \tag{C11}$$

$$z_2 = 4\gamma_0'^2\left\{\gamma_3'^2|g_{\boldsymbol{k}}|^4 + 2\gamma_1'\gamma_3' \mathrm{Re}\left[g_{\boldsymbol{k}}^3\right] + \left(\gamma_1'^2 + 4\Delta^2\right)|g_{\boldsymbol{k}}|^2\right\} + \left(\gamma_3'^2|g_{\boldsymbol{k}}|^2 - \gamma_1'^2\right)^2. \tag{C12}$$

Obviously, the electronic states become electron-hole symmetric. Using Eq. (C10), we can have an analytic discussion of the band gap E_g and the VHS for $\mathcal{J}_{32}$. Around the Dirac point $\boldsymbol{K}$, the approximation $g_{\boldsymbol{k}+\boldsymbol{K}} = -re^{i\theta}$ can be adopted for $\boldsymbol{k} = \frac{2r}{\sqrt{3}a_0}(\cos\theta\hat{\boldsymbol{x}} + \sin\theta\hat{\boldsymbol{y}})$. For zero Δ, the zero energy of $\epsilon_{3\boldsymbol{k}}$ can be directly found from Eq. (C10) at $r = 0$ or $r = r_0 = -\frac{\gamma_1'\gamma_3'}{\gamma_0'^2}$ and $\theta = (2n+1)\pi/3$. Therefore, in total four degenerate zero energy points exist in one Dirac cone at $\Delta = 0$; one is at this Dirac point, and the other three locate along the K-M directions. Furthermore, for small r, $\epsilon_{3\boldsymbol{k}}$ can be approximated by

$$\epsilon_{3\boldsymbol{k}}^2 = \Delta^2 + c_2 r^2 + c_3 \cos(3\theta) r^3 + c_4 r^4, \tag{C13}$$

with

$$c_2 = \gamma_3'^2 - \frac{4\gamma_0'^2\Delta^2}{\gamma_1'^2}, \tag{C14}$$

$$c_3 = -\frac{2\gamma_0'^2\gamma_3'}{\gamma_1'}, \tag{C15}$$

$$c_4 = \frac{\gamma_0'^2}{\gamma_1'^2}\left[\gamma_0'^2 - 2\gamma_3'^2 + \frac{4\Delta^2\left(2\gamma_0'^2 - \gamma_3'^2\right)}{\gamma_1'^2} + \frac{16\gamma_0'^2\Delta^4}{\gamma_1'^4}\right]. \tag{C16}$$

From Eq. (C13) the band structure around the Dirac points has following features:

(1) For nonzero Δ, the energy $\epsilon_{3\boldsymbol{k}}$ at the Dirac point $\boldsymbol{K}$ is an extreme, and it is a local minimum (maximum) as $c_2 > 0$ ($c_2 < 0$), which corresponds to $|\Delta| < \Delta_c$ ($|\Delta| > \Delta_c$), with $\Delta_c = |\gamma_3'\gamma_1'/(2\gamma_0')| = 0.0229\,\mathrm{eV}$.

(2) We first look at the case $|\Delta| > \Delta_c$ ($c_2 < 0$). For a fixed θ, $\epsilon_{3\boldsymbol{k}}$ around the Dirac point $\boldsymbol{K}$ has one more local minimum located at $r = r_e(\cos 3\theta)$, with

$$r_e(\cos 3\theta) = \frac{-3c_3\cos 3\theta + \sqrt{9c_3^2\cos^2 3\theta - 32c_2c_4}}{8c_4}. \tag{C17}$$

When r is fixed and θ varies, $\epsilon_{3\boldsymbol{k}}$ has the local maxima $\cos 3\theta = 1$ and local minima $\cos 3\theta = -1$. When both r and θ are considered, a minimum exists at $r = r_e(-1)$ and $\theta = (2n+1)\pi/3$ (along the K-Γ directions for integer n), and a VHS point exists at $r = r_e(1)$ and $\theta = 2n\pi/3$ (along the K-M directions).

(3) For the case $|\Delta| < \Delta_c$ ($c_2 > 0$), $\epsilon_{3\boldsymbol{k}}$ has no VHS point around the Dirac points, but the minimum along the K-Γ directions still exists.

(4) A similar analysis can be applied to study the JDOS $\mathcal{J}_{42} = \mathcal{J}_{31}$. After ignoring γ_4' and Δ', $\epsilon_{4\boldsymbol{k}} - \epsilon_{2\boldsymbol{k}}$ has a local minimum at the $\boldsymbol{K}$ point, and there is no VHS in $\mathcal{J}_{42}$. Therefore, γ_4' and Δ' play a key role in forming a VHS in $\mathcal{J}_{42}$.

[1] G. B. Osterhoudt, L. K. Diebel, M. J. Gray, X. Yang, J. Stanco, X. Huang, B. Shen, N. Ni, P. J. W. Moll, Y. Ran, and K. S. Burch, Colossal mid-infrared bulk photovoltaic effect in a type-I Weyl semimetal, Nat. Mater. **18**, 471 (2019).

[2] M. O. Sauer, A. Taghizadeh, U. Petralanda, M. Ovesen, K. S. Thygesen, T. Olsen, H. Cornean, and T. G. Pedersen, Shift current photovoltaic efficiency of 2D materials, npj Comput. Mater. **9**, 35 (2023).

[3] J. E. Spanier, V. M. Fridkin, A. M. Rappe, A. R. Akbashev, A. Polemi, Y. Qi, Z. Gu, S. M. Young, C. J. Hawley, D. Imbrenda, G. Xiao, A. L. Bennett-Jackson, and C. L. Johnson, Power conversion efficiency exceeding the Shockley-Queisser limit in a ferroelectric insulator, Nat. Photonics **10**, 611 (2016).

[4] H. M. van Driel and J. E. Sipe, Applications in semiconductors, in *Encyclopedia of Modern Optics*, 2nd ed., edited by B. D. Guenther and D. G. Steel (Elsevier, Oxford, 2005), pp. 486–491.

[5] R. D. R. Bhat and J. E. Sipe, Excitonic effects on the two-color coherent control of interband transitions in bulk semiconductors, Phys. Rev. B **72**, 075205 (2005).

[6] H. T. Duc, J. Förstner, and T. Meier, Microscopic analysis of charge and spin photocurrents injected by circularly polarized one-color laser pulses in GaAs quantum wells, Phys. Rev. B **82**, 115316 (2010).

[7] C. Salazar, J. L. Cheng, and J. E. Sipe, Coherent control of current injection in zigzag graphene nanoribbons, Phys. Rev. B **93**, 075442 (2016).

[8] K. Wang, R. A. Muniz, J. E. Sipe, and S. T. Cundiff, Quantum interference control of photocurrents in semiconductors by nonlinear optical absorption processes, Phys. Rev. Lett. **123**, 067402 (2019).

[9] W. Shockley and H. J. Queisser, Detailed balance limit of efficiency of p-n junction solar cells, J. Appl. Phys. **32**, 510 (1961).

[10] N. T. Kaner, Y. Wei, Y. Jiang, W. Li, X. Xu, K. Pang, X. Li, J. Yang, Y. Jiang, G. Zhang, and W. Q. Tian, Enhanced shift

currents in monolayer 2D GeS and SnS by strain-induced band gap engineering, ACS Omega **5**, 17207 (2020).

[11] A. M. Cook, B. M. Fregoso, F. de Juan, S. Coh, and J. E. Moore, Design principles for shift current photovoltaics, Nat. Commun. **8**, 14176 (2017).

[12] Y. Wei, W. Li, Y. Jiang, and J. Cheng, Electric field induced injection and shift currents in zigzag graphene nanoribbons, Phys. Rev. B **104**, 115402 (2021).

[13] H. Xu, H. Wang, J. Zhou, Y. Guo, J. Kong, and J. Li, Colossal switchable photocurrents in topological Janus transition metal dichalcogenides, npj Comput. Mater. **7**, 31 (2021).

[14] H. Yuan, X. Wang, B. Lian, H. Zhang, X. Fang, B. Shen, G. Xu, Y. Xu, S.-C. Zhang, H. Y. Hwang, and Y. Cui, Generation and electric control of spin-valley-coupled circular photogalvanic current in WSe_2, Nat. Nanotechnol. **9**, 851 (2014).

[15] A. Arora, J. F. Kong, and J. C. W. Song, Strain-induced large injection current in twisted bilayer graphene, Phys. Rev. B **104**, L241404 (2021).

[16] D. Kaplan, T. Holder, and B. Yan, Twisted photovoltaics at terahertz frequencies from momentum shift current, Phys. Rev. Res. **4**, 013209 (2022).

[17] Z. Ji, G. Liu, Z. Addison, W. Liu, P. Yu, H. Gao, Z. Liu, A. M. Rappe, C. L. Kane, E. J. Mele, and R. Agarwal, Spatially dispersive circular photogalvanic effect in a Weyl semimetal, Nat. Mater. **18**, 955 (2019).

[18] C.-K. Chan, N. H. Lindner, G. Refael, and P. A. Lee, Photocurrents in Weyl semimetals, Phys. Rev. B **95**, 041104(R) (2017).

[19] S. M. Young and A. M. Rappe, First principles calculation of the shift current photovoltaic effect in ferroelectrics, Phys. Rev. Lett. **109**, 116601 (2012).

[20] S. Pal, A. B. Swain, P. P. Biswas, D. Murali, A. Pal, B. R. K. Nanda, and P. Murugavel, Giant photovoltaic response in band engineered ferroelectric perovskite, Sci. Rep. **8**, 8005 (2018).

[21] Y. Peng, X. Liu, Z. Sun, C. Ji, L. Li, Z. Wu, S. Wang, Y. Yao, M. Hong, and J. Luo, Exploiting the bulk photovoltaic effect in a 2D trilayered hybrid ferroelectric for highly sensitive polarized light detection, Angew. Chem. **132**, 3961 (2020).

[22] W. Ji, K. Yao, and Y. C. Liang, Bulk photovoltaic effect at visible wavelength in epitaxial ferroelectric $BiFeO_3$ thin films, Adv. Mater. **22**, 1763 (2010).

[23] E. J. Mele, P. Král, and D. Tománek, Coherent control of photocurrents in graphene and carbon nanotubes, Phys. Rev. B **61**, 7669 (2000).

[24] J. L. Cheng, N. Vermeulen, and J. E. Sipe, Third-order nonlinearity of graphene: Effects of phenomenological relaxation and finite temperature, Phys. Rev. B **91**, 235320 (2015).

[25] Z. Zheng, Y. Song, Y. W. Shan, W. Xin, and J. L. Cheng, Optical coherent injection of carrier and current in twisted bilayer graphene, Phys. Rev. B **105**, 085407 (2022).

[26] D. Sun, C. Divin, J. Rioux, J. E. Sipe, C. Berger, W. A. de Heer, P. N. First, and T. B. Norris, Coherent control of ballistic photocurrents in multilayer epitaxial graphene using quantum interference, Nano Lett. **10**, 1293 (2010).

[27] D. Sun, C. Divin, M. Mihnev, T. Winzer, E. Malic, A. Knorr, J. E. Sipe, C. Berger, W. A. De Heer, P. N. First, and T. B. Norris, Current relaxation due to hot carrier scattering in graphene, New J. Phys. **14**, 105012 (2012).

[28] M. Vandelli, M. I. Katsnelson, and E. A. Stepanov, Resonant optical second harmonic generation in graphene-based heterostructures, Phys. Rev. B **99**, 165432 (2019).

[29] S. J. Brun and T. G. Pedersen, Intense and tunable second-harmonic generation in biased bilayer graphene, Phys. Rev. B **91**, 205405 (2015).

[30] K.-H. Lin, S.-W. Weng, P.-W. Lyu, T.-R. Tsai, and W.-B. Su, Observation of optical second harmonic generation from suspended single-layer and bi-layer graphene, Appl. Phys. Lett. **105**, 151605 (2014).

[31] J. Cheng, N. Vermeulen, and J. Sipe, Second order optical nonlinearity of graphene due to electric quadrupole and magnetic dipole effects, Sci. Rep. **7**, 43843 (2017).

[32] Y. Shan, Y. Li, D. Huang, Q. Tong, W. Yao, W.-T. Liu, and S. Wu, Stacking symmetry governed second harmonic generation in graphene trilayers, Sci. Adv. **4**, eaat0074 (2018).

[33] Y. Xiong, L.-K. Shi, and J. C. Song, Atomic configuration controlled photocurrent in van der Waals homostructures, 2D Mater. **8**, 035008 (2021).

[34] S. Chaudhary, C. Lewandowski, and G. Refael, Shift-current response as a probe of quantum geometry and electron-electron interactions in twisted bilayer graphene, Phys. Rev. Res. **4**, 013164 (2022).

[35] Y.-C. Chuang, J.-Y. Wu, and M.-F. Lin, Analytical calculations on low-frequency excitations in AA-stacked bilayer graphene, J. Phys. Soc. Jpn. **81**, 124713 (2012).

[36] J. E. Sipe and A. I. Shkrebtii, Second-order optical response in semiconductors, Phys. Rev. B **61**, 5337 (2000).

[37] C. H. Lui, Z. Li, K. F. Mak, E. Cappelluti, and T. F. Heinz, Observation of an electrically tunable band gap in trilayer graphene, Nat. Phys. **7**, 944 (2011).

[38] N. C. H. Hesp, M. K. Svendsen, K. Watanabe, T. Taniguchi, K. S. Thygesen, I. Torre, and F. H. L. Koppens, WSe_2 as transparent top gate for infrared near-field microscopy, Nano Lett. **22**, 6200 (2022).

[39] T. Ohta, A. Bostwick, T. Seyller, K. Horn, and E. Rotenberg, Controlling the electronic structure of bilayer graphene, Science **313**, 951 (2006).

[40] Y. Gao, Y. Zhang, and D. Xiao, Tunable layer circular photogalvanic effect in twisted bilayers, Phys. Rev. Lett. **124**, 077401 (2020).

[41] F. de Juan, Y. Zhang, T. Morimoto, Y. Sun, J. E. Moore, and A. G. Grushin, Difference frequency generation in topological semimetals, Phys. Rev. Res. **2**, 012017(R) (2020).

[42] L. Gao, Z. Addison, E. J. Mele, and A. M. Rappe, Intrinsic Fermi-surface contribution to the bulk photovoltaic effect, Phys. Rev. Res. **3**, L042032 (2021).

[43] E. McCann and M. Koshino, The electronic properties of bilayer graphene, Rep. Prog. Phys. **76**, 056503 (2013).

[44] T. Rangel, B. M. Fregoso, B. S. Mendoza, T. Morimoto, J. E. Moore, and J. B. Neaton, Large bulk photovoltaic effect and spontaneous polarization of single-layer monochalcogenides, Phys. Rev. Lett. **119**, 067402 (2017).